



Article

Importance of Doping Sequence in Multiple Heteroatom-Doped Reduced Graphene Oxide as Efficient Oxygen Reduction Reaction Electrocatalysts

Jin Hee Kim ¹, Jong Hun Han ¹, Jae-Hyung Wee ², Go Bong Choi ³ , Seungki Hong ^{3,4} and Yoong Ahm Kim ^{3,*}

¹ Optoelectronics Convergence Research Center, School of Chemical Engineering, Chonnam National University, 77 Yongbong-ro, Buk-gu, Gwangju 61186, Korea; jhkimj@chonnam.ac.kr (J.H.K.); jhhan@chonnam.ac.kr (J.H.H.)

² Technical Textile R&D Group, Korea Institute of Industrial Technology, 143 Haggaulro, Sangnok-gu, Ansan-si 15588, Gyeonggi-do, Korea; jhwee0506@gmail.com

³ Department of Polymer Engineering, Graduate School, School of Polymer Science and Engineering & Alan G. MacDiarmid Energy Research Institute, Chonnam National University, 77 Yongbong-ro, Buk-gu, Gwangju 61186, Korea; uppermost.peak@gmail.com (G.B.C.); seungki@kist.re.kr (S.H.)

⁴ Carbon Composite Material Research Center, Korea Institute of Science and Technology (KIST), Jeonbuk 55324, Korea

* Correspondence: yak@chonnam.ac.kr



Citation: Kim, J.H.; Han, J.H.; Wee, J.-H.; Choi, G.B.; Hong, S.; Kim, Y.A. Importance of Doping Sequence in Multiple Heteroatom-Doped Reduced Graphene Oxide as Efficient Oxygen Reduction Reaction Electrocatalysts. *Appl. Nano* **2021**, *2*, 267–277. <https://doi.org/10.3390/applnano2030019>

Academic Editor:
Michalis Konsolakis

Received: 2 July 2021

Accepted: 3 September 2021

Published: 7 September 2021

Publisher's Note: MDPI stays neutral with regard to jurisdictional claims in published maps and institutional affiliations.



Copyright: © 2021 by the authors. Licensee MDPI, Basel, Switzerland. This article is an open access article distributed under the terms and conditions of the Creative Commons Attribution (CC BY) license (<https://creativecommons.org/licenses/by/4.0/>).

Abstract: Multiple heteroatom-doped graphene is of great interest for developing an efficient electrocatalyst for oxygen reduction reaction (ORR). To maximize the electrocatalytic performance of doped graphene, the competitive doping mechanism caused by the different atomic sizes of dopants should be developed. Herein, three different heteroatoms (e.g., N, P and B) are competitively introduced into reduced graphene oxide (RGO) using both single- and two-step processes. The total quantity of heteroatoms for ternary RGO synthesized using the two-step process is lower than that when using the single-step process. Higher ORR electrocatalytic activity for the two-step-synthesized RGO compared to the single-step-synthesized RGO can be explained by: (a) a high amount of P atoms; (b) the fact that B doping itself decreases the less electrocatalytic N moieties such as pyrrole and pyridine and increases the high electrocatalytic moieties such as quaternary N; (c) a high amount of B atoms itself within the RGO act as an electrocatalytic active center for O₂ adsorption; and (d) a small amount of substitutional B might increase the electrical conductivity of RGO. Our findings provide new insights into the design of heteroatom-doped carbon materials with excellent electrocatalytic performance.

Keywords: graphene oxide; heteroatom doping; electrocatalyst

1. Introduction

Identifying efficient catalysts for the cathodic oxygen reduction reaction (ORR) in fuel cells, photocatalytic water splitting, and metal-air batteries has been a critical research direction in recent years [1–5]. Conventionally, noble metals have been considered as the most effective ORR catalysts, but they have experienced several drawbacks such as high cost, poor long-term durability, sluggish electron transfer kinetics, and susceptibility to carbon monoxide poisoning [6–9]. Therefore, active studies regarding the replacement of noble metal-based catalysts with efficient and inexpensive non-metal catalysts have been carried out [10].

Among many types of carbon materials, two-dimensional graphenes have been examined as efficient catalysts owing to their large surface area, high electrical conductivity, and good chemical stability. However, pure graphene with no bandgap exhibited limited electrocatalytic activity due to the low number of active sites. Therefore, to generate electrocatalytic active sites within the graphene and improve its electrocatalytic activity, it is highly recommended to incorporate heteroatom elements (e.g., nitrogen (N) [11,12], boron (B) [13],

phosphor (P) [14,15], and sulfur (S) [16,17]) into the graphene as heteroatom doping introduces defects, increases both interlayer spacing and electrical conductivity of graphene, and eventually can act as active sites. Recent works reported that dual-doped graphene with two types of heteroatoms (e.g., BN [18,19], NS [20–22], and NP [23–25]) exhibited improved electrocatalytic activity due to their synergistic effect compared to single-atom-doped graphene. These results indicate the potential of multiple-doped graphene for use as metal-free electrocatalysts. The ternary-doped graphene that uses three different heteroatom elements (e.g., NPB) [26] exhibited excellent ORR activity that was comparable to commercially available Pt catalysts. Therefore, the competitive doping mechanism of three different atoms with regard to the hosting material should be elucidated to maximize their electrocatalytic performance, especially by considering the doping sequence of the heteroatom elements.

The main distinguishing feature of graphene oxide is the presence of a high density of defects within the graphene matrix [27]. When considering the simultaneous thermal reduction and heteroatom introduction in the thermal doping process as well as the electrocatalytic reaction occurring on its exposed surface, it is critical to understand how the three different atoms are competitively introduced within the graphene network or at the edge of the graphene homogeneously or heterogeneously depending on the doping sequence. In the present work, ternary-doped reduced graphene oxides (RGOs) were synthesized by a two-step process using DNA and B_2O_3 as sources and evaluated as electrocatalysts for ORRs. Graphene oxide was thermally reduced with the simultaneous introduction of N and P atoms using DNA, which has nitrogen-containing nucleobases and phosphorus groups. Then, additional doping with B was carried out using B_2O_3 as the source. The atomic sizes of the three different atoms led to their relative proportion and configurations within RGO, thereby resulting in the altered electrocatalytic activity of the catalysts for ORRs. Thus, the doping sequence should be optimized to maximize the electrocatalytic performance of ternary doped graphenes.

2. Materials and Methods

2.1. Preparation of Ternary-Doped RGO

GO powder used in our study was purchased from Grapheneall Co., LTD (Siheung, Republic of Korea). N, P, and B-doped RGO (denoted NPBRGO) was prepared by thermally doping P and N atoms into RGO using DNA as the dopant, followed by B doping using the thermal diffusion method. Firstly, N and P co-doped RGO (denoted NPRGO) was obtained by thermally treating a GO/DNA mixture at 800 °C in argon. GO (100 mg) was dissolved in distilled water (20 mL) using a bath-type sonicator for 1 h. Then, DNA (100 mg) was added to the GO solution. After freeze-drying the GO/DNA solution, the solid-state mixture was heated to 800 °C in argon. After washing several times using distilled water and then drying at 60 °C for one day, grey-colored NPRGO powder was obtained. Secondly, to incorporate B atoms into NPRGO, we selected B_2O_3 as dopant. The NPRGO and B_2O_3 (wt. ratio = 1:0.5) were mixed using a mortar and pestle, and the mixture was thermally treated at 1000 °C for 1 h. To remove the residual B_2O_3 , the reactant was refluxed in a 3M NaOH solution for 2 h. After washing the reactant several times using distilled water and then drying at 60 °C for one day, black-colored N, P, and B-doped RGO powder was obtained. For comparison, we also prepared N, P, and B-doped RGO by heating the GO, DNA, and B_2O_3 mixture to 1000 °C in argon using a single-step process.

2.2. Structural Characterizations

The structure and surface morphology of samples were characterized by field emission scanning electron microscopy (FESEM, Gemini 500) and high-resolution transmission electron microscopy (HRTEM, Titan3 G2 operated with 80 kV). Elemental mapping (EELS) was obtained by monochromated TEM (FEI-Titan Cubed) with Dual EELS (Gatan quantum 963). Energy resolution was 0.2 eV in 80 kV of experimental condition. Dispersion is 0.1 eV/ch and dwell time is 1 s/pixel. To evaluate the chemical configuration of the pristine and

heteroatom-doped RGO, X-ray photoelectron spectroscopy (XPS, K-Alpha, ThermoFisher Scientific, Waltham, MA, USA) was used. Raman spectroscopy (Renishaw Invia, 514 nm laser) was used to evaluate the structural integrity of NPRGO and NPBRGO samples. The pore structure of doped RGOs were investigated via N₂ adsorption measurements at 77 K using volumetric equipment (BELSROP-max, MicrotracBEL, Tokyo, Japan) after pre-evacuation for 6 h at 393 K, while the pressure was maintained at 10⁻² Pa.

2.3. Electrochemical Analysis

Electrochemical measurements using cyclic voltammetry (CV) and linear sweep voltammograms (LSV) were performed with a standard three-electrode system using an Autolab potentiostat/galvanostat. Ag/AgCl (3 M KCl) electrode and Pt wire were used as the reference electrode and counter electrode, respectively. The working electrode was prepared by loading carbon-based catalysts obtained by dispersing 10 mg of carbon materials into the mixture of 1 mL ethanol and 100 µL Nafion (5% *w/w* solution) and sonicating for 30 min. Then, 5 µL of the dispersed carbon materials was loaded onto a glassy carbon electrode (GCE) and dried at room temperature. Cyclic voltammetry (CV) and linear sweep voltammetry (LSV) using a rotating disk electrode (RDE) were measured in an O₂-or N₂-saturated 0.1 M KOH electrolyte with a sweep rate of 5 mV/s. Before the measurement, the GCE was purged at flow rate of 30 mL/min for 30 min. The conversion of the potential to reversible hydrogen electrode (RHE) was expressed by the following equation.

$$E_{(RHE)} = E_{Ag/AgCl} + 0.059 \text{ pH} + E^{\circ}_{Ag/AgCl}$$

where $E^{\circ}_{Ag/AgCl} = 0.1976 \text{ V}$ (at 25 °C)

The electron-transfer number (*n*) per oxygen molecule was obtained using the Koutecky-Levich (K-L) equation [28,29].

$$1/J = 1/(B\omega^{1/2}) + 1/J_K$$

where, *J* is the measured current density, *J_K* is the kinetic limiting-current density, and ω is the rotational speed of the electrode. The parameter *B* could be determined from the slope of the K-L plots from the Levich equation.

$$B = 0.62 nFC_0(D_0)^{2/3}(\nu)^{-1/6}$$

where, *n* is the electron transfer number, *F* is the Faraday constant ($F = 96,485 \text{ C mol}^{-1}$), *C₀* is the bulk concentration of O₂ ($C_0 = 1.2 \times 10^{-6} \text{ mol/cm}^3$), *D₀* is the diffusion coefficient of O₂ in KOH solution ($D_0 = 1.9 \times 10^{-5} \text{ cm}^2/\text{s}$), ν is the kinematic viscosity of the electrolyte ($\nu = 0.01 \text{ cm}^2/\text{s}$) and, 0.62 is a constant used to express the rotational speed in rad/s.

Thus, *n* can be deduced from the slope of the linear plot of J^{-1} versus $\omega^{-1/2}$ (K-L plot).

3. Results and Discussion

When GO was subjected to thermal doping, the color of the material changed from dark brown to black, indicating thermal reduction by the removal of oxygen functionalities. The effect of doping on the morphological changes of heteroatom-doped RGO was evaluated using SEM and TEM and the elemental distribution within the RGO was verified using EELS elemental mapping. As shown in Figure 1a–d and Figure S1a–d, both samples exhibited similar characteristics, such as sheet-like morphology and wrinkled and folded microtextures. These corrugations may be attributed to the introduction of heteroatoms into the graphene matrix. In addition, there is no distinctive difference in microtexture between NPRGO and NPBRGO depending on the quantity and type of heteroatoms. The homogeneous introduction of N, P, and B atoms into the graphene matrix were identified from EELS elemental mapping images of ternary doped RGO obtained using two-step (Figure 1e–i) and one-step (Figure S2a–e), respectively.

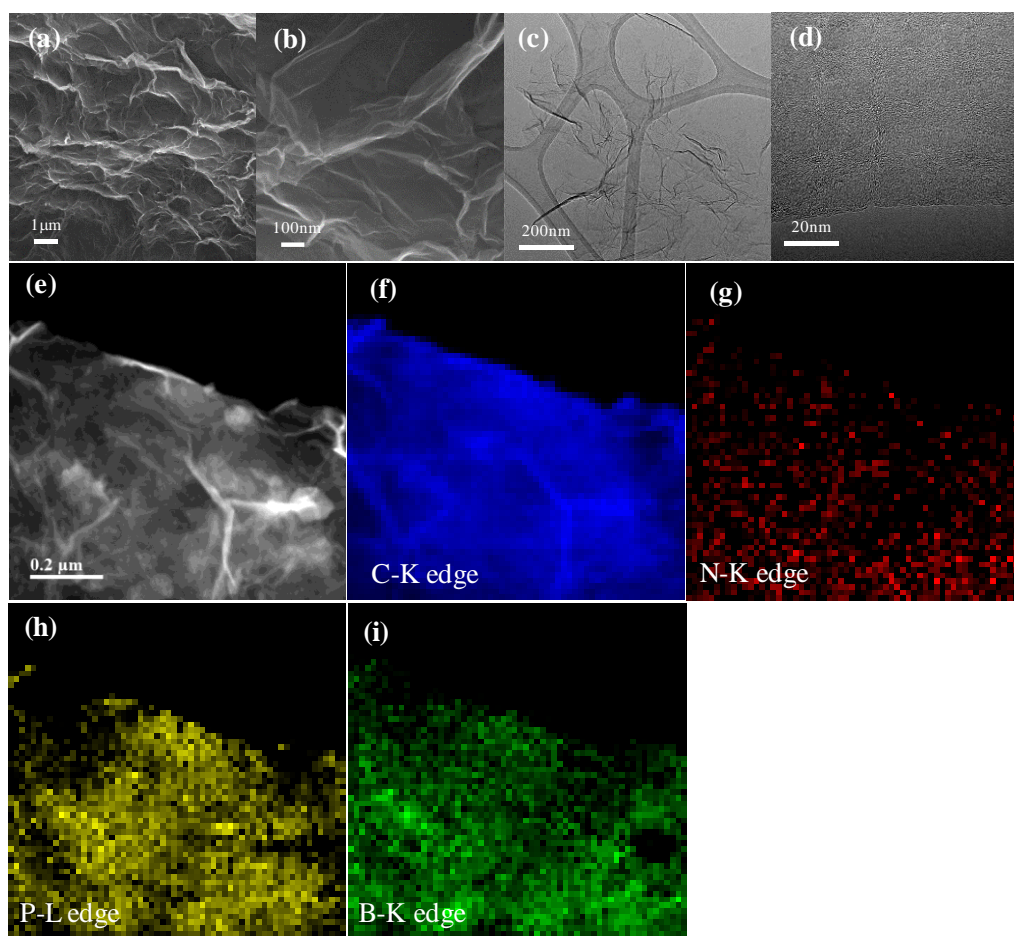


Figure 1. SEM (a,b) and TEM (c,d) images of ternary doped RGO using two-step method. Note that the sheet-like graphenes are corrugated and wrinkled. (e) Elastic TEM image and EELS elemental mapping images of (f) carbon, (g) nitrogen, (h) phosphorous, and (i) boron atoms.

To understand the effect of the doping sequence on the electrocatalytic performance of RGO, we prepared ternary doped RGO using both single-step and two-step methods. GO showed a substantial weight loss at 200 °C due to the decomposition of the liable oxygen functional group (Figure S3a), while subsequent weight loss could be attributed to the decomposition of stable oxygen functional groups with increasing temperature. More specifically, the decomposition temperatures of carboxyl (CO₂), acid anhydride (CO and CO₂), lactone (CO₂), ether and hydroxyl (CO), and quinone and carbonyl (CO) were identified at 300, 500, 700, 800, and 1000 °C, respectively. However, DNA decomposed above 200 °C (Figure S3b) while B₂O₃ has a melting point of 450 °C. Thus, in the case of one-step doping, three different elements were competitively involved in the doping process of the defective graphene matrix below 500 °C. Therefore, it is highly desirable to characterize the doped quantity of heteroatoms and their bonding configurations using XPS. From the wide scan XPS spectra (Figure 2a), the observation of peaks at 285.4, 532.3, 400.4, 191 and 134 eV, which can be assigned to C 1s, O 1s, N 1s, B 1s, and P 2p, indicates the successful introduction of N, P and B atoms into RGO. The relative quantities are summarized in Table 1. In the case of two-step doping, the structurally and thermally stabilized N, P dual-doped RGO might interact with B₂O₃. In the two-step sample, we observed a low amount of N (ca. 3.02 at %), B atoms (ca. 3.90 at %) and a high amount of P (ca. 2.36 at %) as compared with the single-step case (Table 1). It is expected that the N atoms, which are smaller than C atoms, are more easily incorporated while the larger P and B atoms competed with each other. In addition, we observed a clear difference in bonding configurations of N, P, and B atoms via comparative studies on narrow scan N 1s, P 2p and

B 1s XPS spectra of NPBRGO (single-step) and NPBRGO (two-step) (Figure 2b–d). The B 1s spectra (Figure 2b) can be deconvoluted into three peaks at 189.3, 190.8 and 192.4 eV, which are assigned to substitutional boron, BCO_2 , BC_2O and B_2O_3 , respectively [30]. The N 1s spectra (Figure 2c) consists of four peaks at 398.5, 399.8, 401.1 and 403.0 eV, which are assigned to pyridinic, pyrrolic, quaternary N and oxidized N, respectively [31,32]. The P 2p peak (Figure 2d) is deconvoluted into three peaks at 134.2, 132.4 and 133.5 eV, which can be assigned to P-O, P-N and P-C bonds, respectively [33]. The relative number of bonding configurations for ternary doped RGOs obtained using single-step and two-step methods are summarized in Table S1.

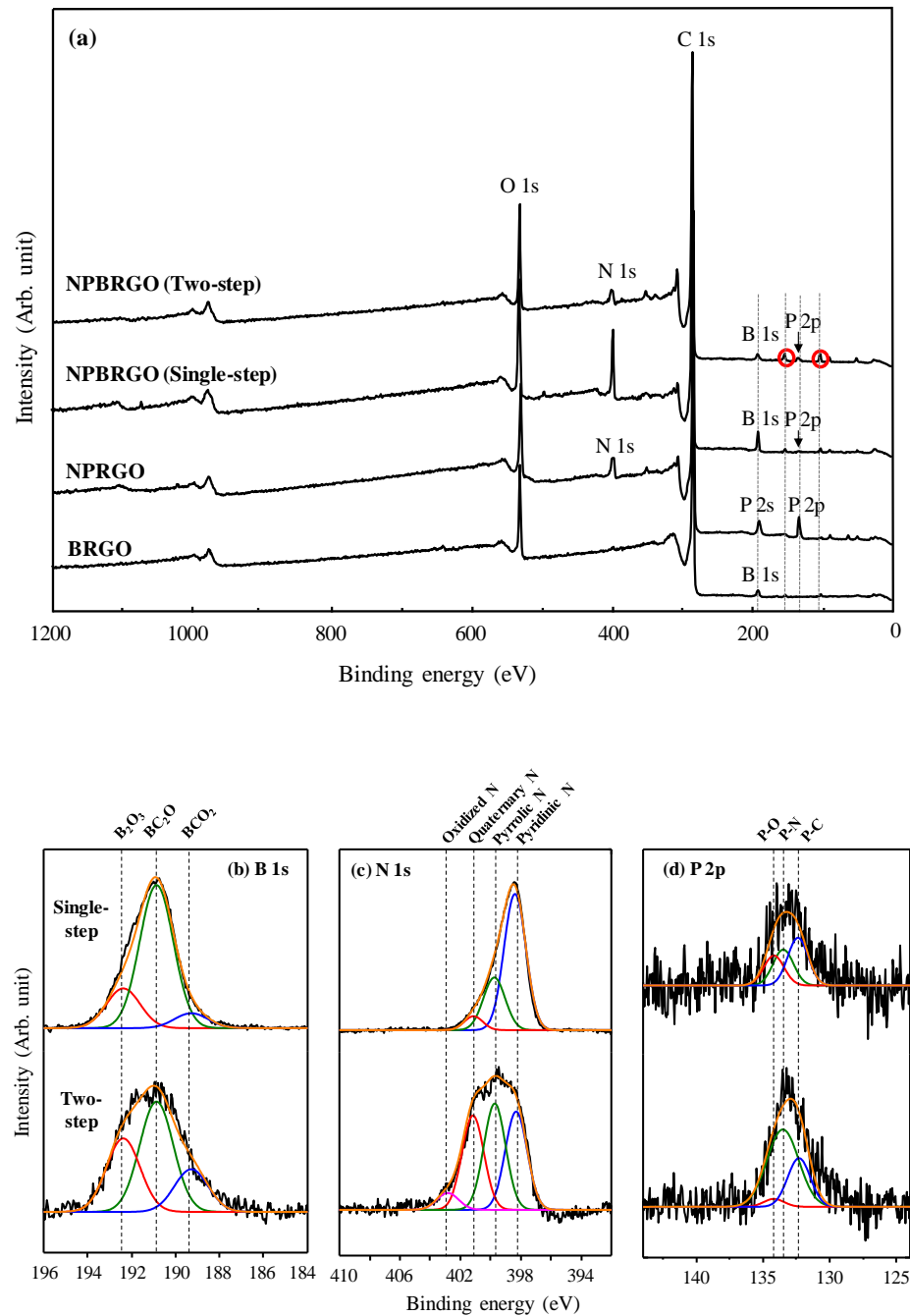


Figure 2. (a) Wide scan XPS spectra of BRGO, NPRGO, NPBRGO (single-step) and NPBRGO (two-step) and narrow scan (b) B 1s, (c) N 1s and (d) P 2p XPS spectra of NPBRGO (single-step) and NPBRGO (two-step). Note that B 1s and P 2s peaks are exactly overlapped and two small peaks owing to the B atoms were clearly observed at around 140 and 100 eV.

Table 1. Atomic composition of ternary doped reduced graphene oxides using both single-step and two-step methods.

I.D.	Atomic %				
	C	O	N	P	B
Single-step	68.77	14.93	6.85	1.01	8.44
Two-step	77.50	13.23	3.02	2.36	3.90

When considering the region in the vicinity of 200 eV, the B 1s peak in the range from 187 to 196 eV for B-doped RGO nearly overlaps the P 2s peak in the range from 186 to 195 eV (Figure S4). Therefore, when the P 2s peak is larger than the B 1s peak, the B 1s peak is completely hidden by the P 2s peak (Figure S4). In contrast, when the B 1s peak is larger than P 2s peak, P 2s is hidden. Therefore, the quantity of B in the ternary doped RGO was not evaluated exactly because the P 2s and B 1s peaks overlap completely. Intrinsically, such issues can be ascribed to the low sensitivity for the B 1s peak. Therefore, to identify the successful introduction of B atoms into the N, P dual-doped RGO, the XPS spectra of NPRGO corresponding to various temperatures in the range from 400 to 1000 °C is compared directly with the XPS spectrum of NPBRGO that are prepared using two step doping (Figure S5). In the case of the P-doped RGO, the relative intensity of the P 2s peak is lower than that of P 2p. However, the relative intensities of the P 2s peak and P 2p peak were clearly changed when B atoms are introduced into N, P co-doped RGO. In this case, the intensity of the B 1s peak exceeds that of the P 2s peak. Therefore, we can conclude that such a peak can be assigned to B 1s. Moreover, we observed two small peaks around 150 and 100 eV (Figure 2a) which may be attributed to the B atoms within RGO. Those results with the elemental mapping of B (see Figure 1i) strongly support our claim regarding the successful doping of N, P, and B heteroatoms into the RGO.

The structural integrity of the doped RGO was evaluated by the Raman spectra using 532 nm laser line (Figure 3a) [34]. There are two major peaks at 1340 cm^{-1} (defect-induced mode, D-band) and 1580 cm^{-1} (E_{2g2} , G-band) for ternary doped RGOs. To evaluate the degree of disorder caused by heteroatom doping, FWHM (full width at half maximum), the R value (I_D/I_G , the integrated intensity of the D-band is divided by the integrated intensity of the G-band) and $I_D/(I_D + I_G)$ are directly compared (see Table S2) [35,36]. We would like to emphasize the relatively intensified D band, the low FWHM value and the high R value for the NPBRGO prepared using two-step doping compared with NPBRGO synthesized by single-step doping. Because B atoms have a three times higher diffusion rate than C atoms, the decorated B moieties on the edge of the RGO might remove the less stable N moieties while sustaining the P moieties and thus diffuse into the hexagonal lattice of graphene, resulting in a highly intensified D band in the Raman spectrum. The specific surface area of ternary doped RGOs were determined by N_2 adsorption/desorption isotherms (Figure S6). The N_2 adsorption isotherms of doped RGOs were found to be combined I and IV. The specific surface area of ternary doped RGOs is 7 m^2/g for single-step and 20 m^2/g for two-step, respectively. Therefore, it is expected that the effect of specific surface area on the electrocatalytic performance might be minimum. The effect of the doping sequence on the electrocatalytic performance of the ternary doped RGO was evaluated by cyclic voltammetry (CV) in an N_2 or O_2 -saturated 0.1M KOH electrolyte (Figure 3b). When the electrolyte is saturated with N_2 , we observed featureless CV within the ORR potential range. In case of O_2 -saturated electrolyte, we observed a positive shift in the cathodic peak for two-step NPBRGO when compared with that of single-step NPBRGO. These results signify that electrocatalytic activity of the two-step NPBRGO is higher than that of single-step NPBRGO. The effect of doping sequence on the electrocatalytic performance of ternary doped RGO was additionally evaluated by measuring linear sweep voltammetry (LSV) curves (Figure 3c,e). Both samples exhibited only one limiting current density, similar to the reference Pt/C sample. The continuous linear increase in the limiting current density with increasing rotation rate indicates the

concomitant increase in oxygen diffusion on the surface of the electrode. We observed a higher onset voltage for the two-step synthesized RGO (ca. 0.89 V) compared to single-step synthesized RGO (ca. 0.8 V), indicating the substantial increase in the availability of ORR active sites due to the presence of the high proportion of P atoms with the help of B atoms. The higher limiting current density for the two-step synthesized RGO can be explained by the well-known catalytic graphitization function of the B atoms with regard to carbon materials [37,38]. As a reference, we obtained the LSV curves for B-doped and N, P codoped RGOs (Figures S7 and S8). The onset voltage of the B-doped and N, P codoped RGOs were 0.83 V and 0.85 V, indicating that the positive shift in the onset potential of the two-step synthesized RGO can be explained by the enhanced ORR activity coming from the synergistic effect of three different heteroatoms. In addition, their K-L plots (Figure 3d,f) are obtained from their LSV curves in the range from 0.2 to 0.6 V. A good linearity signifies a first-order reaction with regard to the concentration of dissolved oxygen [22]. From the inset of Figure 4f, the number of electrons transferred in the range from 2.82 to 3.52 for two-step synthesized NPBRGO is slightly higher than that of the single-step synthesized NPBRGO (Figure 4). This result indicates an efficient electron-transfer process for the oxygen reduction reaction on two-step synthesized NPBRGO electrode. In order to evaluate the durability of two-step synthesized RGOs, chronoamperometric measurements were performed at 0.7 V in an O₂-saturated 0.1 M KOH solution compared with 20 wt.% Pt/C (Figure S9). Ternary doped RGOs showed a higher long-term stability in comparison with 20 wt.% Pt/C for 10,000 s.

Furthermore, to understand the effect of N, P and B doping on the electrocatalytic activity of RGO, we compared CV of two-step synthesized RGO with that of B- and N, P codoped RGOs (Figure 4a). The CV curve for undoped RGO showed a near-rectangular shape whereas we observed broad reversible peaks for the doped RGOs. In addition, we observed a positive shift in the cathodic peak for two-step synthesized NPBRGO when compared with those of RGO and NPRGO. These results signify that electrocatalytic activity of the NPBRGO improved considerably compared with NPRGO and RGO. It is expected that the strong affinity of the heteroatom-doped graphene toward oxygen will facilitate the O₂ adsorption [39,40]. It is well known that the phenol group and the deprotonation of the carboxyl group in the KOH electrolyte contribute to the quasi-reversible pseudo-capacitance. However, there is no considerable difference in the quantity of O atoms between NPRGO and NPBRGO according to the XPS study (Table S3). Thus, such a possibility can be discarded. We observed a large increase in the current density for NPBRGO when compared to NPRGO and undoped RGO. Such an increase can be explained by the pseudo-capacitance of the N, P, and B moieties, especially when decorated on the RGO edges [41,42]. To further investigate the ORR activities of the doped RGO samples, LSV curves using a rotating disk electrode (RDE) was obtained in an O₂-saturated 0.1 M KOH electrolyte at a speed of 1600 rpm (Figure 4b). The onset potential of NPBRGO was positively shifted compared to that of NPRGO and RGO without a decrease in the limiting current density. The LSV curve of RGO shows two-step two-electron pathway with the formation of superoxide (HO₂⁻) as an intermediate, while NPRGO and NPBRGO show a combination of two- and four-electron pathways involving in the ORR process [43–46]. Therefore, we can say that N, P, and B ternary-doped RGO shows much better ORR electrocatalytic activity than the dual-doped and undoped RGO.

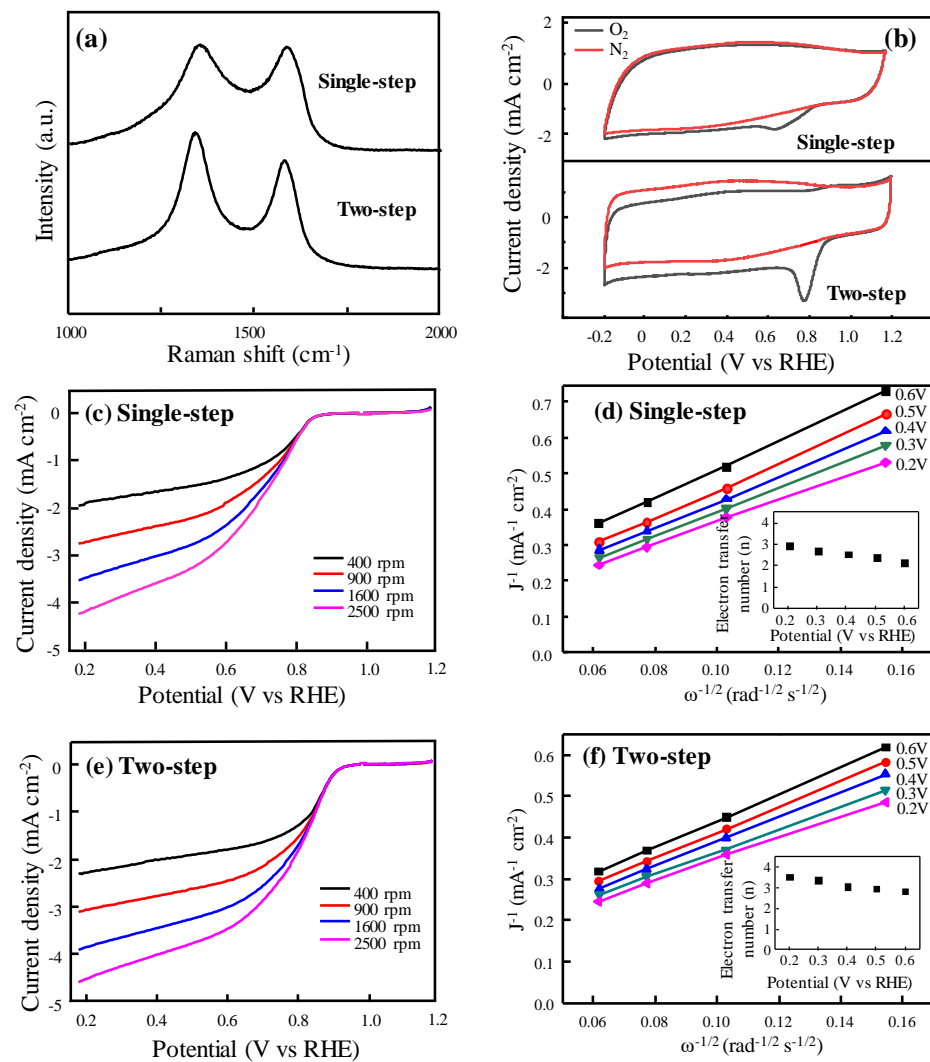


Figure 3. (a) Raman spectra and (b) cyclic voltammograms of ternary doped RGOs using single-step and two-step methods using a scan rate of 50 mV/s in N₂ or O₂ saturated 0.1 M KOH solution. Linear sweep voltammograms of ternary doped RGOs using (c) single-step and (e) two-step synthesis, obtained in a O₂-saturated 0.1 M KOH aqueous electrolyte using different rotation speeds (scan rate of 5 mV/s) and (d,f) their K-L plots in the range from 0.2 to 0.6 V (inset is the electron transfer number at different potential).

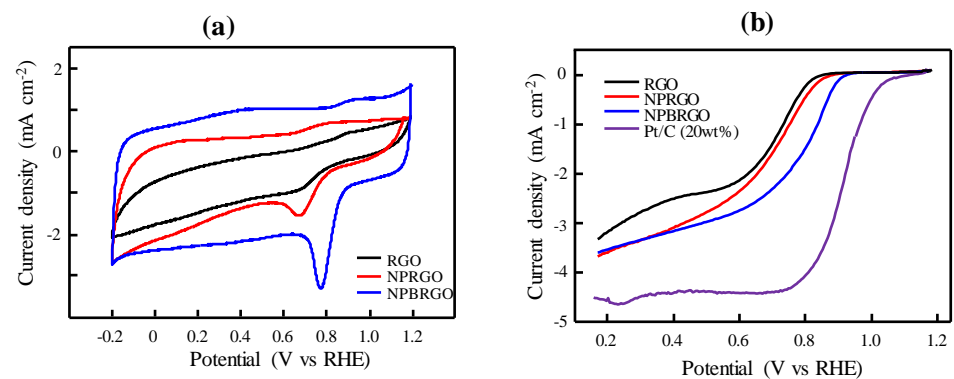


Figure 4. (a) Cyclic voltammograms of RGO, NPRGO, and NPBRGO using a scan rate of 50 mV/s in an O₂ saturated 0.1 M KOH solution, (b) linear sweep voltammograms of RGO, NPRGO, and NPBRGO (reference = Pt/C (20 wt.%)) using a rotational speed of 1600 rpm.

4. Conclusions

Ternary doped RGOs containing N, P, and B atoms were synthesized by a two-step doping process that uses DNA and B₂O₃ as dopant sources, and multiple-doped RGOs were evaluated as electrocatalysts for ORRs. Dark brown colored GO was thermally reduced to black colored RGO at 800 °C in argon by simultaneously introducing N and P atoms from the DNA. The additional B doping was carried out by thermal doping using B₂O₃ at 1000 °C in argon. The total quantity of heteroatoms for the two-step synthesized ternary RGO (ca. 9.3 at %) is considerably lower than that of the single-step synthesized ternary RGO (ca. 16.3 at %). However, we observed a higher ORR electrocatalytic activity from the two-step RGO than from the single-step RGO due to the higher amount of P. When considering the overlap of the B 1s and P 2p XPS spectra, the amount of P within the two-step ternary RGO is assumed to be ca. 2.36 at %. Even though the heteroatoms within the graphene matrix can induce charge redistribution and create more catalytic active sites, their relative concentration as well as configurations is quite important to maximize the electrocatalytic performance of the multiple-heteroatom-doped graphenes.

Supplementary Materials: The following are available online at <https://www.mdpi.com/article/10.3390/applnano2030019/s1>. Figure S1: SEM (a,b) and TEM (c,d) images of N, P codoped reduced graphene oxides at different magnification; Figure S2: TEM image and EELS elemental mapping images of ternary doped reduced graphene oxide obtained using one-step method: (a) elastic TEM image and (b) carbon, (c) nitrogen, (d) phosphorus and (e) boron atoms; Figure S3: Thermogravimetric curves of (a) graphene oxide and (b) graphene oxide and DNA mixture in argon atmosphere and their derivatives; Figure S4: P 2s and B 1s spectra of ternary doped reduced graphene oxide using two-step; Figure S5: Comparative XPS spectra of N, P dual doped RGO that are prepared at different temperatures and ternary doped reduced graphene oxide; Figure S6: Nitrogen adsorption/desorption isotherms of ternary doped RGOs obtained using single-step and two-step methods; Figure S7 Linear sweep voltammograms of boron doped RGO obtained in 0.1 M O₂-saturated KOH electrolyte using different rotation speeds and their K-L plots in the range from 0.2 to 0.6 V (inset is the electron transfer number at different potential); Figure S8: Linear sweep voltammograms of N, P co doped reduced graphene oxide obtained in 0.1 M O₂-saturated KOH electrolyte using different rotation speeds; Table S1: Relative amount of bonding configurations of three heteroatoms for ternary doped reduced graphene oxides obtained using single-step and two-step methods; Table S2: Raman parameter of ternary doped reduced graphene oxides obtained using one-step and two-step methods; Table S3: Atomic composition of dual and ternary doped reduced graphene oxides.

Author Contributions: Conceptualization, J.H.K.; methodology, J.-H.W., G.B.C. and S.H.; investigation, J.H.K.; data curation, G.B.C. and S.H.; writing—original draft preparation, J.H.K. and J.H.H.; writing—review and editing, Y.A.K.; supervision, Y.A.K.; project administration, Y.A.K. All authors have read and agreed to the published version of the manuscript.

Funding: J.H.K. acknowledges the financial support from Basic Science Research Program through the National Research Foundation of Korea (NRF) funded by the Ministry of Education (2021R111-A1A01057335). Y.A.K. acknowledge the financial support from Basic Science Research Program through the National Research Foundation of Korea (NRF) funded by the Ministry of Education (2021R111A305628711). J.H.H. acknowledges financial support from Priority Research Centers Program through the National Research Foundation of Korea (NRF) funded by the Ministry of Education, Science and Technology (2018R1A6A1A03024334).

Institutional Review Board Statement: Not applicable.

Informed Consent Statement: Not applicable.

Conflicts of Interest: The authors declare no conflict of interest.

References

1. Takanabe, K. Photocatalytic water splitting: Quantitative approaches toward photocatalyst by design. *ACS Catal.* **2017**, *7*, 8006–8022. [[CrossRef](#)]
2. Strasser, P. Free electrons to molecular bonds and back: Closing the energetic oxygen reduction (ORR)-oxygen evolution (OER) cycle using core-shell nanoelectrocatalysts. *Acc. Chem. Res.* **2016**, *49*, 2658–2668. [[CrossRef](#)]

3. Yadegari, H.; Norouzi Banis, M.; Lushington, A.; Sun, Q.; Li, R.; Sham, T.K.; Sun, X. A bifunctional solid state catalyst with enhanced cycling stability for Na and Li-O₂ cells: Revealing the role of solid state catalysts. *Energy Env. Sci.* **2017**, *10*, 286–295. [[CrossRef](#)]
4. Wang, Z.L.; Xu, D.; Xu, J.J.; Zhang, X.B. Oxygen electrocatalysts in metal-air batteries: From aqueous to nonaqueous electrolytes. *Chem. Soc. Rev.* **2014**, *43*, 7746–7786. [[CrossRef](#)]
5. Yan, Y.; Shin, W.I.; Chen, H.; Lee, S.-M.; Manickam, S.; Hanson, S.; Zhao, H.; Lester, E.; Wu, T.; Pang, C.H. A recent trend: Application of graphene in catalyst. *Carbon Lett.* **2021**, *31*, 177–199. [[CrossRef](#)]
6. Debe, M.K. Electrocatalyst approaches and challenges for automotive fuel cells. *Nature* **2012**, *486*, 43–51. [[CrossRef](#)]
7. Steele, B.C.H.; Heinzel, A. Materials for fuel-cell technologies. *Nature* **2001**, *414*, 345–352. [[CrossRef](#)]
8. Serov, A.; Kwak, C. Review of non-platinum anode catalysts for DMFC and PEMFC application. *Appl. Catal.* **2009**, *90*, 313–320. [[CrossRef](#)]
9. Sun, Y.Q.; Wu, Q.O.; Shi, G.Q. Graphene based new energy materials. *Energy Environ. Sci.* **2011**, *4*, 1113–1132. [[CrossRef](#)]
10. Liu, X.; Dai, L. Carbon-based metal-free catalysts. *Nat. Rev. Mater.* **2016**, *1*, 16064. [[CrossRef](#)]
11. Zhao, Y.; Hu, C.G.; Hu, Y.; Cheng, H.H.; Shi, G.Q.; Qu, L.T. A versatile, ultralight, nitrogen-doped graphene framework. *Angew. Chem. Int. Ed.* **2012**, *51*, 11371–11375. [[CrossRef](#)]
12. Lai, L.; Potts, J.R.; Zhan, D.; Wang, L.; Poh, C.K.; Tang, C.; Gong, H.; Shen, Z.; Lin, J.; Ruoff, R.S. Exploration of the active center structure of nitrogen-doped graphene-based catalysts for oxygen reduction reaction. *Energy Environ. Sci.* **2012**, *5*, 7936–7942. [[CrossRef](#)]
13. Zhou, Y.Z.; Yen, C.H.; Fu, S.F.; Yang, G.H.; Zhu, C.Z.; Du, D.; Wo, P.C.; Cheng, X.N.; Yang, J.; Wai, C.M.; et al. One-pot synthesis of b-doped three-dimensional reduced graphene oxide via supercritical fluid for oxygen reduction reaction. *Green Chem.* **2015**, *17*, 3552–3560. [[CrossRef](#)]
14. Li, R.; Wei, Z.D.; Gou, X.L.; Xu, W. Phosphorus-doped graphene nanosheets as efficient metal-free oxygen reduction electrocatalysts. *RSC Adv.* **2013**, *3*, 9978–9984. [[CrossRef](#)]
15. Zhang, C.Z.; Mahmood, N.; Yin, H.; Liu, F.; Hou, Y.L. Synthesis of phosphorus-doped graphene and its multifunctional applications for oxygen reduction reaction and lithium ion batteries. *Adv. Mater.* **2013**, *25*, 4932–4937. [[CrossRef](#)]
16. Yang, Z.; Yao, Z.; Li, G.F.; Fang, G.Y.; Nie, H.G.; Liu, Z.; Zhou, X.M.; Chen, X.; Huang, S.M. Sulfur-doped graphene as an efficient metal-free cathode catalyst for oxygen reduction. *ACS Nano* **2012**, *6*, 205–211. [[CrossRef](#)]
17. Chen, X.; Chen, X.H.; Xu, X.; Yang, Z.; Liu, Z.; Zhang, L.J.; Xu, X.J.; Chen, Y.; Huang, S.M. Sulfur-doped porous reduced graphene oxide hollow nanosphere frameworks as metal-free electrocatalysts for oxygen reduction reaction and as supercapacitor electrode materials. *Nanoscale* **2014**, *6*, 13740–13747. [[CrossRef](#)]
18. Gong, Y.J.; Fei, H.L.; Zou, X.L.; Zhou, W.; Yang, S.B.; Ye, G.L.; Liu, Z.; Peng, Z.W.; Lou, J.; Vajtai, R.; et al. Boron- and nitrogen-substituted graphene nanoribbons as efficient catalysts for oxygen reduction reaction. *Chem. Mater.* **2015**, *27*, 1181–1186. [[CrossRef](#)]
19. Pei, Y.; Song, H.; Liu, Y.; Cheng, Y.; Li, W.; Chen, Y.; Fan, Y.; Liu, B.; Lu, S. Boron-nitrogen-doped carbon dots on multi-walled carbon nanotubes for efficient electrocatalysis of oxygen reduction reactions. *J. Colloid Interface Sci.* **2021**, *600*, 865–871. [[CrossRef](#)]
20. Ai, W.; Luo, Z.M.; Jiang, J.; Zhu, J.H.; Du, Z.Z.; Fan, Z.X.; Xie, L.H.; Zhang, H.; Huang, W.; Yu, T. Nitrogen and sulfur codoped graphene: Multifunctional electrode materials for high performance Li-ion batteries and oxygen reduction reaction. *Adv. Mater.* **2014**, *26*, 6186–6192. [[CrossRef](#)]
21. Zhao, Y.; Hu, C.G.; Song, L.; Wang, L.X.; Shi, G.Q.; Dai, L.M.; Qu, L.T. Functional graphene nanomesh foam. *Energy Environ. Sci.* **2014**, *7*, 1913–1918. [[CrossRef](#)]
22. Xu, J.X.; Dong, G.F.; Jin, C.H.; Huang, M.H.; Guan, L.H. Sulfur and nitrogen co-doped, few-layered graphene oxide as a highly efficient electrocatalyst for the oxygen reduction reaction. *ChemSusChem* **2013**, *6*, 493–499. [[CrossRef](#)] [[PubMed](#)]
23. Choi, C.H.; Chung, M.W.; Kwon, H.C.; Park, S.H.; Woo, S.I. B, N- and P, N-doped graphene as highly active catalysts for oxygen reduction reactions in acidic media. *J. Mater. Chem. A* **2013**, *1*, 3694–3699. [[CrossRef](#)]
24. Wang, C.L.; Zhou, Y.; Sun, L.; Zhao, Q.; Zhang, X.; Wan, P.; Qiu, J.S. N/P-codoped thermally reduced graphene for high-performance supercapacitor applications. *J. Phys. Chem. C* **2013**, *117*, 14912–14919. [[CrossRef](#)]
25. Li, R.; Wei, Z.D.; Gou, X.L. Nitrogen and phosphorus dual-doped graphene/carbon nanosheets as bifunctional electrocatalysts for oxygen reduction and evolution. *ACS Catal.* **2015**, *5*, 4133–4142. [[CrossRef](#)]
26. Lin, H.L.; Chu, L.; Wang, X.J.; Yao, Z.Q.; Liu, F.; Ai, Y.N.; Zhuang, X.D.; Han, S. Boron, nitrogen, and phosphorus ternary doped graphene aerogel with hierarchically porous structure as highly efficient electrocatalysts for oxygen reduction reaction. *N. J. Chem.* **2016**, *40*, 6022–6029. [[CrossRef](#)]
27. Feicht, P.; Eigler, S. Defects in graphene oxide as structural motifs. *ChemNanoMat* **2018**, *4*, 244–252. [[CrossRef](#)]
28. Wang, S.Y.; Yu, D.S.; Dai, L.M.; Chang, D.W.; Baek, J.B. Polyelectrolyte-functionalized graphene as metal-free electrocatalysts for oxygen reduction. *ACS Nano* **2011**, *5*, 6202–6209. [[CrossRef](#)]
29. Paulus, U.A.; Wokaun, A.; Scherer, G.G.; Schmidt, T.J.; Stamenkovic, V.; Radmilovic, V.; Markovic, N.M.; Ross, P.N. Oxygen reduction on carbon-supported Pt-Ni and Pt-Co alloy catalyst. *J. Phys. Chem. B* **2002**, *106*, 4181–4191. [[CrossRef](#)]
30. Fujisawa, K.; Hayashi, T.; Endo, M.; Terrones, M.; Kim, J.H.; Kim, Y.A. Effect of boron doping on the electrical conductivity of metallicity-separated single walled carbon nanotubes. *Nanoscale* **2018**, *10*, 12723. [[CrossRef](#)]
31. Maldonado, S.; Morin, S.; Stevenson, K.J. Structure, composition, and chemical reactivity of carbon nanotubes by selective nitrogen doping. *Carbon* **2006**, *44*, 1429–1437. [[CrossRef](#)]

32. Pels, J.; Kapteijn, F.; Moulijn, J.; Zhu, Q.; Thomas, K. Evolution of nitrogen functionalities in carbonaceous materials during pyrolysis. *Carbon* **1995**, *33*, 1641–1653. [[CrossRef](#)]
33. Wu, J.; Zheng, X.; Jin, C.; Tian, J.; Yang, R. Ternary doping of phosphorus, nitrogen, and sulfur into porous carbon for enhancing electrocatalytic reduction. *Carbon* **2015**, *92*, 327–338. [[CrossRef](#)]
34. Chadha, N.; Sharma, R.; Saini, P. A new insight into the structural modulation of graphene oxide upon chemical reduction probed by Raman spectroscopy and X-ray diffraction. *Carbon Lett.* **2021**. [[CrossRef](#)]
35. Cuesta, A.; Dhameincourt, P.; Laureyns, J.; Martinez-Alonso, A.; Tascon, J.M.D. Raman microprobe studies on carbon materials. *Carbon* **1994**, *32*, 1523–1532. [[CrossRef](#)]
36. Panomsuwan, G.; Saito, N.; Isizaki, T. Electrocatalytic oxygen reduction on nitrogen-doped carbon nanoparticles derived from cyano-aromatic molecules via a solution plasma approach. *Carbon* **2016**, *98*, 411–420. [[CrossRef](#)]
37. Ha, S.; Choi, G.B.; Hong, S.; Kim, D.W.; Kim, Y.A. Substitutional boron doping on carbon materials. *Carbon Lett.* **2018**, *27*, 1–11.
38. Shin, Y.; Park, S. Production of B-doped reduced graphene oxide using wet-process in tetrahydrofuran. *Carbon Lett.* **2020**, *27*, 1–11. [[CrossRef](#)]
39. Liu, Z.W.; Peng, F.; Wang, H.J.; Yu, H.; Xheng, W.X.; Yang, J. Phosphorus-doped graphite layers with high electrocatalytic activity for the O₂ reduction in an alkaline medium. *Angew. Chem. Int. Ed.* **2011**, *50*, 3257–3261. [[CrossRef](#)]
40. Zhao, G.; Shi, L.; Xu, J.B.; Yan, X.O.; Zhao, T.S. Role of phosphorus in nitrogen, phosphorus dual-doped ordered mesoporous carbon electrocatalyst for oxygen reduction reaction in alkaline media. *Int. J. Hydrogen. Energy* **2018**, *43*, 1470–1478. [[CrossRef](#)]
41. Fujisawa, K.; Cruz-Silva, R.; Yang, K.-S.; Kim, Y.A.; Hayashi, T.; Endo, M.; Terrones, M.; Dresselhaus, M.S. Importance of open, heteroatom-decorated edges in chemically doped-graphene for supercapacitor applications. *J. Mater. Chem. A* **2014**, *2*, 9532–9540. [[CrossRef](#)]
42. Yang, B.; Zhang, D.; He, J.; Wang, Y.; Wang, K.; Li, H.; Wang, Y.; Miao, L.; Ren, R.; Xie, M. Simple and green fabrication of a biomass-derived N and O self-doped hierarchical porous carbon via a self-activation route for supercapacitor application. *Carbon Lett.* **2020**, *30*, 709–719. [[CrossRef](#)]
43. Zhang, J.T.; Xia, Z.H.; Dai, L.M. Carbon-based electrocatalysts for advanced energy conversion and storage. *Sci. Adv.* **2015**, *1*, 1–19. [[CrossRef](#)] [[PubMed](#)]
44. Norskov, J.K.; Rossmeisl, J.; Logadottir, A.; Lindqvist, L.; Kitchin, J.R.; Bligaard, T.; Jonsson, H. Origin of the overpotential for oxygen reduction at a fuel-cell cathode. *J. Phys. Chem. B* **2004**, *108*, 17886–17892. [[CrossRef](#)]
45. Xu, H.; Cheng, D.; Cao, D.; Zeng, X.C. A universal principle for a rational design of single-atom electrocatalysts. *Nat. Catal.* **2018**, *1*, 339–348. [[CrossRef](#)]
46. Jiang, Z.; Alexandrov, V. Enhancing Oxygen Electroreduction Activity of Single-Site Fe–N–C Catalysts by a Metal Support. *J. Phys. Chem. C* **2019**, *123*, 30335–30340. [[CrossRef](#)]